Cell Communication and Signaling

RESEARCH Open Access

EMT induction in normal breast epithelial cells by *COX2*-expressing fibroblasts

Minwoo Kang[1], Somayadineshraj Devarasou[1], Nam Ji Sung[1], Tae Yoon Kwon[1] and Jennifer H. Shin[1,2,3*]

Abstract

Background The tumor microenvironment (TME) plays a pivotal role in cancer progression, with cancer-associated fibroblasts (CAFs) significantly influencing tumor behavior. Especially, elevated *COX2* expressing fibroblasts within the TME, notably in collagen-dense tumors like breast cancer, has been recently emphasized in the literature. However, the specific effect of *COX2*-expressing CAFs ($COX2^+$ CAFs) on neighboring cells and their consequent role in cancer progression is not fully elucidated.

Methods We induced $COX2^+$ fibroblasts by forcing the fibroblasts forming aggregates to undergo Nemosis as a proxy for $COX2^+$ CAFs. This approach enabled us to simulate the paracrine interactions between $COX2^+$ CAFs and normal breast epithelial cells via conditioned media from $COX2^+$ fibroblasts. We developed an innovative in vitro platform that combines cell mechanics-based analysis and biomolecular assays to study the interactions between $COX2^+$ fibroblasts and normal breast epithelial cells. By focusing on the mechanical characteristics of the cells and the epithelial-mesenchymal transition (EMT) marker expressions, we aimed to elucidate the paracrine mechanisms through which $COX2^+$ CAFs influence the tumor microenvironment.

Results Our in vitro findings demonstrate that $COX2^+$ fibroblasts, through conditioned media, induce significant alterations in the mechanical behavior of normal breast epithelial cells, as evidenced by monolayer expansion measurements using traction force microscopy (TFM). This transition was further corroborated by single-cell morphology and motility analyses, as well as increased expression of mesenchymal markers, including *SNAI1* at the mRNA level and vimentin at the protein level. EP4 inhibition partially reversed these changes, preserving cell-cell interactions, limiting monolayer expansion, and reducing mesenchymal-like features, suggesting that PGE2–EP4 signaling plays a key role in mediating the paracrine effects of $COX2^+$ fibroblasts. Together, our findings support a model in which PGE2–EP4 signaling contributes to EMT induction, potentially involving *SNAI1* regulation, with implications for targeting stromal-epithelial interactions in breast cancer.

Conclusion This study advances our understanding of the potential mechanisms by which $COX2^+$ CAFs influence tumor progression within the breast tumor microenvironment (TME) through controlled in vitro investigations. By integrating cell mechanics-based analysis, biomolecular assays, and innovative in vitro cell-based modeling of $COX2^+$ CAFs, we have delineated the contributory role of these cells in a controlled setting. These insights lay a groundwork for future studies that could explore the implications of these findings in vivo, potentially guiding targeted therapeutic strategies.

*Correspondence:
Jennifer H. Shin
j_shin@kaist.ac.kr

Full list of author information is available at the end of the article

Keywords Fibroblasts, Cancer-associated fibroblasts, *COX2*, Nemosis, PGE2, EMT, Breast cancer, Tumor microenvironment

Introduction

The tumor microenvironment (TME) is a complex ecosystem of various cells, including immune cells, endothelial cells, and most notably, fibroblasts, all of which play a crucial role in shaping the evolutionary path of tumors through continuous interaction and signaling with cancer cells [1–4]. Among these, fibroblasts, particularly in their activated form known as cancer-associated fibroblasts (CAFs), are emerging as key contributors to tumor progression. CAFs have a well-documented role in promoting cancer progression through both physical and molecular interactions [5]. Studies, such as those by Zhang et al. [6], highlight their involvement in processes like aggregate formation and epithelial-mesenchymal transition (EMT). By orchestrating changes in the extracellular matrix (ECM) and secreting growth factors, CAFs support cancer cell survival and metastasis during tumor development.

The EMT is a critical process in cancer metastasis and progression, wherein epithelial cells acquire mesenchymal characteristics, resulting in a loss of epithelial traits and an increase in migratory capabilities. Epithelial cells, characterized by specific cell junctions such as adherens junctions, gap junctions, and apical-basal polarity, undergo significant changes during EMT, losing these features and adopting back-front polarity indicative of enhanced migratory function [7]. While EMT is widely recognized in contexts such as embryonic morphogenesis and wound healing, it is particularly well-studied in cancer biology [8]. As cancer advances, epithelial cancer cells begin to exhibit mesenchymal traits, becoming more invasive through EMT activation [9–12]. However, this transition is not a binary switch between fully epithelial and fully mesenchymal states [8]. Cells often express a combination of both epithelial and mesenchymal markers, making it challenging to fully capture this phenotypic spectrum through biomarkers alone. To gain a more comprehensive understanding of EMT, it is essential to consider additional factors, such as the biophysical characteristics of the cells, which may provide deeper insights into the complexity and heterogeneity of this process.

Prostaglandin-endoperoxide synthase 2 (*PTGS2*), commonly referred to as cyclooxygenase-2 (*COX2*), is the gene responsible for prostaglandin biosynthesis [13]. Two isoforms of cyclooxygenase exist in humans: *COX1*, which is constitutively expressed in most tissues and regulates the conversion of arachidonic acid to prostaglandins for routine physiological functions [14], and *COX2*, which is induced during inflammatory responses and is typically absent in normal cells. *COX2* is widely recognized as a biomarker for various cancers [15, 16], [17], with elevated levels serving as a distinguishing indicator of tumor presence. Overexpression of *COX2* in cancer cells not only promotes carcinogenesis but also correlates with poorer patient survival [18–22], contributing to increased resistance to chemotherapy and radiotherapy [23, 24].

Recent research has highlighted the presence of high *COX2* expression within the tumor microenvironment (TME), particularly in collagen-dense tumors and cancers such as colorectal, intestinal, and nasopharyngeal cancers [25–28]. Additionally, a significant association has been found between *COX2*-expressing breast tumors and the number of cancer-associated fibroblasts (CAFs) [29]. In colorectal cancer, CAFs have been identified as the main sources of both *COX2* and prostaglandin E2 (PGE2) [30, 31]. Despite this, the impact of elevated stromal *COX2* expression or *COX2*-expressing CAFs ($COX2^+$ CAFs) on neighboring cells and tumor progression remains insufficiently explored.

PGE2, the end product of *COX2* activity, is a key mediator of inflammation and tissue regeneration. Like *COX2*, persistently elevated levels of PGE2 are strongly linked to various human malignancies. Numerous studies suggest that PGE2 plays a role in promoting cancer cell growth, proliferation, survival, angiogenesis, and metastasis [32–35], making it a potential prognostic biomarker for cancer [36–38]. PGE2 exerts its effects through four E-series prostaglandin receptors (EP 1–4), engaging in autocrine and paracrine signaling, with responses varying across different cell and tissue types. For instance, while PGE2 inhibits the EMT in Madin-Darby canine kidney (MDCK) cells, it promotes EMT in nasopharyngeal cancer cells [27, 39, 40].

Nemosis is a process in which fibroblasts become activated and form clusters under certain in vitro conditions [41]. Under normal physiological conditions, fibroblasts, being mesenchymal cells, typically do not form aggregates. However, when exposed to tumor-derived paracrine factors, fibroblasts can be induced to cluster into aggregates that closely resemble the nemosis state observed in vitro. For instance, fibroblasts have been shown to form spheroids in response to Bowes melanoma line-conditioned medium [42]. Although the term nemosis has not been definitively documented in vivo, indirect evidence supports the occurrence of fibroblast aggregation in multiple tumor types. In melanoma, fibroblast aggregates can form at tumor sites through paracrine interactions, suggesting that a nemosis-like process might occur in the tumor stroma [43–45]. Furthermore,

fibroblast clusters have also been detected in other cancers, including lung metastases, where stromal fibroblasts co-travel with metastatic tumor cells and provide structural and growth advantages [46]. Similarly, in metastatic breast cancer, CAFs have been identified circulating alongside circulating tumor cells (CTCs), potentially forming clusters that enhance tumor progression and metastasis [47]. Nemosis is characterized by elevated levels of *COX2*, as well as upregulated secretion of growth factors including VEGF, HGF, and FGF7 [48, 49]. As previously noted, while *COX1* is consistently expressed in most tissues, *COX2* is typically absent in normal tissues and becomes rapidly upregulated in response to inflammation [41]. These properties closely align with several features of CAFs—especially those described in inflammatory and tumor-promoting contexts. Based on this, $COX2^+$ fibroblasts undergoing nemosis were used as a model for $COX2^+$ CAFs, given their accessibility and the ability to study cellular mechanisms in a controlled environment, while acknowledging the complexity and heterogeneity of CAF behavior in vivo.

To explore the paracrine signaling dynamics between $COX2^+$ fibroblasts and neighboring normal breast epithelial cells, we simulated these interactions using conditioned media from $COX2^+$ fibroblasts, also referred to as nemotic fibroblasts (NF). Enzyme-linked immunosorbent assay (ELISA) revealed that the conditioned media from $COX2^+$ fibroblasts (NF) contained elevated levels of PGE2, the primary product of *COX2*, compared to the negative control. Further analysis demonstrated that the NF-induced conditioned media (Nemo-CM) were capable of initiating EMT in normal breast epithelial cells. A combination of cell mechanics-based approaches and biomolecular assays was used to assess EMT. The findings of this study support the hypothesis that PGE2, derived from $COX2^+$ fibroblasts in the tumor stroma, can drive the EMT of normal breast epithelial cells, providing strong evidence for a positive feedback mechanism involved in breast cancer progression.

Materials and methods

Cell culture and preparation of conditioned media

MCF10A cells (ATCC No.CRL-10317) were cultured in DMEM/F12(GIBCO) supplemented with 5% horse serum (Invitrogen 16050-122), 500 ng/ml hydrocortisone (Sigma-Aldrich H0888), 100 ng/ml cholera toxin (Sigma-Aldrich C8052), 20 ng/ml epidermal growth factor (EGF, Peprotech), 10 µg/ml insulin (Sigma-Aldrich I1882), and 1% penicillin-streptomycin (PS, Invitrogen 15070-063). Human adult dermal fibroblasts (HDFs, Lonza) were cultured in DMEM (WelGene) supplemented with 10% fetal bovine serum (FBS, WelGene), and 1% penicillin-streptomycin (WelGene).

To induce nemosis, 100 µl of cell suspension drops, containing 1×10^4 HDFs, were seeded on Ultra-Low Attachment 96 well plate (Corning). Each well contained one fibroblast spheroid. After four days of culture, the media (Nemo) were collected and filtered before use (0.2 µm Nalgene syringe filter). For negative control media from flat 96 well plate (Control), thesame amount of cell suspension drops was seeded, and the media were collected and filtered before use (Fig.1a).

To assess the specific contribution of PGE2 to EMT-related changes, MCF10A cells were treated with control conditioned media (Control) supplemented with exogenous PGE2. Prostaglandin E2 (PGE2; Sigma-Aldrich, P0409) was dissolved according to the manufacturer's instructions and added to the Control at a final concentration of 8.51 nM (equivalent to 3,000 pg/ml). Cells were incubated with the PGE2-supplemented media (Control + PGE2) for 48 h before collection for protein analysis via Western blot.

Enzyme-linked immunosorbent assay

To quantify PGE2 concentrations in conditioned media, conditioned media (control and Nemo) were collected after 4 days of culture. PGE2 concentrations in the conditioned media were measured by an enzyme-linked immunosorbent assay (ELISA) kit (Prostaglandin E2 Parameter Assay Kit, KGB, R&D Systems) according to the manufacturer's instructions.

Polyacrylamide gel preparation

Cells were cultured on masked polyacrylamide (PA) gel substrates (Young's modulus = 3 kPa, thickness = 100 µm) that were prepared following the protocols as previously described [50]. Briefly, the 24 µl of PA gel drop mixed with red fluorescent beads (diameter = 0.5 µm; FluoSpheres; Life Technologies) was polymerized in a silane-treated glass bottom dish (Spl) under a cover slip (diameter = 18 mm; VWR). The PA gel surface was functionalized with 1 mg/ml of Sulfo-SANPAH (sulfosuccinimidyl-6-(4-azido-2-nitrophenylamino) hexanoate) in warm 50 mM HEPES buffer (Life Technologies) for immobilization of 100 µg/ml collagen type I (PureCol, Advanced BioMatrix).

Cell monolayer patterning and time-lapse microscopy

Cellular islands were patterned for cell monolayer expansion using polydimethylsiloxane (PDMS; Sylgard 184; Dow Corning) stencil with 700 µm-diameter holes. The PDMS stencil was coated with 2% Pluronic F-127 solution (Sigma-Aldrich) at 37 °C for 1 h. The prepared PDMS stencil was placed on the PA gel substrate. 200 µl aliquot of MCF10A cell-suspension (density = 5×10^5 cells/ml) was loaded on the pattern. The sample was then incubated at 37 °C / 5% CO_2 for 30 min, a duration

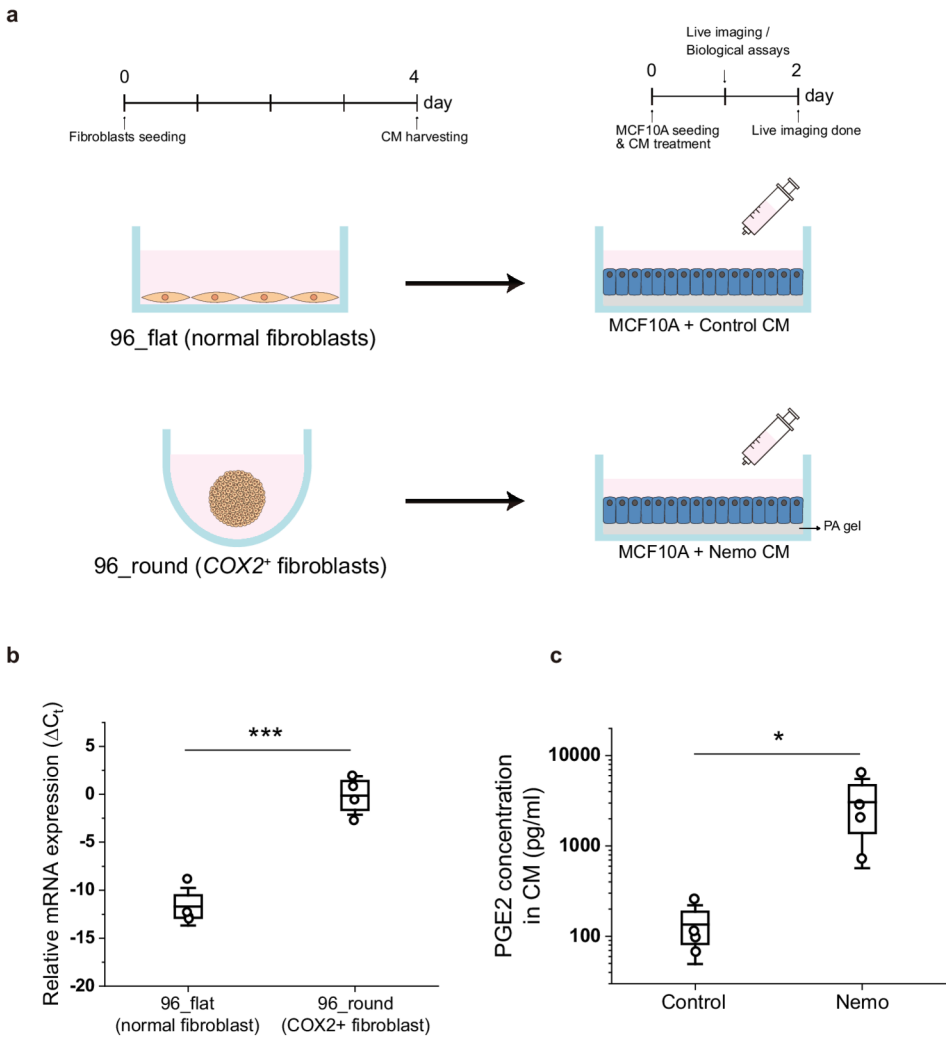

Fig. 1 Mimicking paracrine signaling of *COX2*$^+$ fibroblasts in vitro. (**a**) Schematic diagram of experimental design. (**b**) mRNA expression level of *COX2* of fibroblasts cultured on 96-well flat-bottom (96_flat) and 96-well round-bottom (96_round) cell culture plates. $n=4$ (**c**) PGE2 concentrations in conditioned media (CM) harvested from 96-well flat-bottom (Control) and 96-well round-bottom (Nemo) cell culture plates. $n=4$. Statistical significance is denoted as follows: $p<0.05$ (*), $p<0.001$ (***)

selected based on prior studies indicating that MCF10A cells effectively adhere and stabilize on polyacrylamide gel surfaces within this timeframe. To confirm that cells remain consistently retained during media exchange, we performed microscopic observations before and after media replacement and found no significant detachment or loss of cells. After the cell stabilization, cell-suspension was drained to remove the floating cells then conditioned media was treated for 24 h (control and Nemo) (Fig. 1(a)). All experiments were performed on the Axio Observer. Z1/7 (Carl Zeiss) microscope equipped with a climate-controlled chamber (37 °C and 5% CO_2). Phase-contrast and fluorescence images were taken every 10 min for 24 h using a 5x objective lens and 1x optovar magnification changer (Carl Zeiss).

Fourier transform traction microscopy (FTTM) and monolayer stress microscopy (MSM)

Tractions of the cellular monolayer were measured using the unconstrained Fourier transform traction microscopy (FTTM) with corrections for substrates of finite thickness, as described in previous reports [51–53]. To calculate monolayer stress, we used the monolayer stress microscopy (MSM) approach, which is detailed by previously published references [54, 55]. Briefly, intercellular stress was calculated based on the balance of tractions across the cellular monolayer according to Newton's second law. The principal stresses, $\sigma_{\max}$ and $\sigma_{\min}$, can be converted from the internal stress tensor. For each local point on the cellular monolayer, the local average normal stress σ_{mean} is defined as $(\sigma_{min}+\sigma_{max})/2$, and it represents the scalar tension within the monolayer.

$$\sigma_{mean} = \frac{\sigma_{max} + \sigma_{min}}{2} = \frac{\sigma_{xx} + \sigma_{yy}}{2} = \frac{\sigma_{rr} + \sigma_{\theta\theta}}{2}$$

Single-cell morphological and migratory features quantification

Morphological features of single-cell images were quantified with *imageJ* [56] by manually tracking the cell boundary. The aspect ratio, circularity, and solidity were calculated with the following expressions.

$$\text{Aspect ratio} = \frac{major\ axis}{minor\ axis}$$

$$\text{Circularity} = \frac{4\pi * area}{perimeter^2}$$

$$\text{Solidity} = \frac{area}{convex\ area}$$

To quantify the migratory features of single-cells, the centroids of single cells were manually tracked with *ImageJ*. After acquiring the centroids of single cells of time series image stacks, mean-squared displacement (MSD), instantaneous speed, and directional ratio were calculated.

Immunofluorescence and the EP4 antagonist

Cells were washed with 1X DPBS (Dulbecco's Phosphate buffered saline, Welgene) and fixed for 15 min in 4%(v/v) paraformaldehyde. After washing three times with PBS, cells were permeabilized by 0.2% (v/v) Triton X-100 (Sigma- Aldrich) for 10 min and blocked by 3% (v/v) bovine serum albumin (BSA) for 1 h in 4°C. After washing in PBS, cells were incubated with diluted primary antibody (Anti-Vimentin, 1:100, BD Pharmingen™ #550513) overnight, followed by the incubation with secondary antibodies (Alexa Fluor 488, 1:100, Invitrogen) for 1 hour in room temperature. Actin filaments were stained with phalloidin (Alexa Fluor 568-phalloidin, 1:100, Invitrogen). For nucleus staining, 4',6-diamidino-2-phenylindole (DAPI, 1:50,000, Molecular Probe) was incubated with in the cells for 3 min at room temperature. Cells were then imaged using multichannel fluorescence microscopy (Carl Zeiss).

The EP4 receptor antagonist L-161,982 (SML0690, Sigma-Aldrich) was used for the PGE2 receptor inhibition study. For monolayer expansion experiments, MCF10A cells were first seeded and incubated for 30 min with MCF10A culture media for attachment. Then, the attached cells were pre-incubated with serum-free media (DMEM supplemented with 1% PS) with either dimethyl sulfoxide (DMSO) only or L-161,982 (10 μM in DMSO) for preincubation of 1 h. After the preincubation, cells were washed with PBS and cultured with Nemo-CM for 24 h.

Western blot

Cells were washed with cold PBS and lysed on ice for 30 minutes using Cell Lysis Buffer (#9803, Cell Signaling Technology, USA). The lysates were then centrifuged at 12,000 rpm for 15 minutes at 4 °C, and the supernatant was collected. Protein concentrations were determined using the Bradford (Coomassie) Protein Assay Plus Kit (#P7200-050, GenDEPOT, USA). Equal amounts of protein were separated by SDS-PAGE on a 10% polyacrylamide gel and transferred onto PVDF membranes (#IPVH00010, Merck Millipore, USA). Membranes were blocked and incubated overnight at 4 °C with primary antibodies against EP4 (sc-55596, Santa Cruz Biotechnology, USA), Snail (#3879S, Cell Signaling Technology, USA), Vimentin (#550513, BD Biosciences, USA), and GAPDH (#2118S, Cell Signaling Technology, USA). Following washes, membranes were incubated with HRP-conjugated secondary antibodies (#7074S and #7076S, Cell Signaling Technology, USA) for 1 hour at room temperature. Bands were visualized using Westsave Gold chemiluminescent reagent (#32109, Thermo Scientific™, USA), and intensity values were quantified using ImageJ (NIH, USA). Outliers in protein band intensity (normalized to GAPDH) were identified and excluded using the interquartile range (IQR) method, defined as values falling outside 1.5 times the IQR above the third quartile or below the first quartile.

Quantitative reverse transcription PCR

At the end of the experiments, total RNA was isolated from fibroblasts or MCF10A cells with RNAiso Plus reagent (Takara Bio, Japan) according to the manufacturer's instructions. Extracted RNAs were reverse transcribed to cDNA using iScript cDNA Synthesis Kits (Bio-Rad, USA) and Biometra T-personal Thermal Cycler for the synthesis. Quantitative Reverse transcription PCR (qRT-PCR) was carried out in duplicates with iQ SYBR green supermix (Bio-Rad, USA) and a Bio-Rad CFX96, real-time detection system. Glyceraldehyde 3-phosphate dehydrogenase (GAPDH) was used for the reference gene. ΔCt values were used to quantify relative mRNA expression and for hypothesis testing. ΔCt was calculated as: ΔCt = Ct(reference gene) − Ct(gene of interest), where Ct is the threshold cycle.

The following primers were used:

GAPDH (For: CTGGGCTACACTGAGCACC, Rev: AAGTGGTCGTTGAGGGCAATG), COX-2 (For: CTGGCGCTCAGCCATACAG, Rev: CGCACTTATACTGGTCAAATCCC), CDH1 (For: CGAGAGCTACACGTTCACGG, Rev: GGGTGTCGAGGGAAAAATAGG), CDH2 (For: TCAGGCGTCTGTAGAGGCTT, Rev: ATGCACATCCTTCGATAAGACTG), VIM (For: AGTCCACTGAGTACCGGAGAC, Rev: CATTTCACGCATCTGGCGTTC), SNAI1 (For: TCGGAAGCCTAACTACAGCGA,

Rev: AGATGAGCATTGGCAGCGAG), SNAI2 (For: CGAACTGGACACACATACAGTG, Rev: CTGAGGATCTCTGGTTGTGGT), TWIST (For: GTCCGCAGTCTTACGAGGAG, Rev: GCTTGAGGGTCTGAATCTTGCT), ZEB1 (For: GATGATGAATGCGAGTCAGATGC, Rev: ACAGCAGTGTCTTGTTGTTGT), ZEB2 (For: CAAGAGGCGCAAACAAGCC, Rev: GGTTGGCAATACCGTCATCC).

Statistical analysis

We assessed the normality of our data using the Shapiro-Wilk test. For hypothesis testing, the Student's t-test or Mann-Whitney U test was used depending on the normality of the data. P-values < 0.05 were considered as statistically significant. Statistical significance is denoted as follows: $p < 0.05$ (*), $p < 0.01$ (**), and $p < 0.001$ (***). Statistical tests were performed using *jamovi* version 1.6.23.0 (The jamovi project (2021), https://www.jamovi.org).

Results

Validation of the simulated *COX2*$^+$ fibroblasts through fibroblast aggregates by the comparative expression of *COX2* of fibroblast aggregates and PGE2 concentrations in conditioned media

To evaluate the validity of using *COX2*$^+$ fibroblasts formed via in vitro aggregation of fibroblasts as a proxy for *COX2*$^+$ CAFs, we first constructed the fibroblast aggregates by culturing the fibroblasts on the low-attachment surface of 96-well round-bottom cell culture plates. Then, *COX2* expression level was checked within fibroblast aggregates and PGE2 concentrations in conditioned media. For the control group, the same number of fibroblasts were cultured on the standard 96-well flat-bottom cell culture plates (Fig. 1a).

To determine *COX2* expression level in fibroblasts, qRT-PCR was performed on the fourth day of culture, which confirmed a significantly higher mRNA expression of *COX2* in aggregated fibroblasts cultured on a low-attachment surface (96_round) compared to those cultured in 2D on a normal surface (96_flat) (Fig. 1b). Next, ELISA analysis confirmed the significantly elevated PGE2 concentrations in the conditioned media (CM) harvested from *COX2*$^+$ fibroblasts (Nemo-CM) (Fig. 1c). These results suggest that Nemo-CM can serve as a surrogate for mimicking the paracrine interactions between *COX2*$^+$ CAFs and neighboring cells within the TME. To further investigate the impact of this simulated signaling on tumor microenvironment dynamics, we exposed normal breast epithelial MCF10A cells—a model widely used for studying breast cancer genetics [57–59]—to both control and Nemo-CM, and observed their phenotypic changes from cell-mechanical and biomolecular perspectives.

The collective behavior of cells implies the EMT of normal breast epithelial cells via Nemo-CM

To observe the collective behavior of cells, we established monolayer circles using MCF10A cells. The cells were patterned in circular islands on collagen I-coated polyacrylamide (PA) gel using a PDMS stencil of a circular shape. After cells settled on the hydrogel, the culture medium was changed to CM (control or Nemo). After 24 h, the stencil was removed to allow cells to settle and form a coherent monolayer (Fig. 2a). When the monolayer came into contact with free space due to stencil removal, the patterned cells began to expand radially. We identified a distinctive behavior of monolayers with different CM conditions (Fig. 2b-g). MCF10A monolayers cultured with Nemo-CM expanded much faster and more aggressively (Supplementary Video 1). We quantified the expansion of monolayers after 16 h of expansion (Fig. 2b). In addition to the expansion speed, we verified the different cell-cell interactions under various conditions. At the 16-hour mark, snapshots revealed disrupted cell-cell interactions in the Nemo-CM-treated sample. In contrast, the control group maintained robust cell-cell contacts (Fig. 2c), supporting the phenotypic transition of cells when cultured with Nemo-CM. The cells appeared to have undergone EMT based on the increased migratory capacity and the loss of stable cell-cell interactions. To further investigate the biophysical characteristics of cellular monolayers, we employed Fourier transform traction microscopy (FTTM) and monolayer stress microscopy (MSM) to analyze tractions and intercellular stresses (Fig. 2d-g). These techniques are particularly valuable in evaluating EMT as they provide dynamic, real-time measurements of cellular forces, offering insights beyond traditional endpoint assays [60–62].

At the initial point of the free expansion, Nemo-CM-treated monolayers showed higher inward traction force (blue-colored) at the edge compared to the control group, indicating that cells at the edge are pulling themselves toward the free space (Fig. 2d). In addition, the Nemo-CM-treated group also had more inward traction regions in the center core, evidenced by more blue-colored area, which suggests that cells at the core also endeavored to migrate outward like the expanding front. This trend was maintained throughout the experiment. This result supports our speculation on EMT and aligns with the previous report that TGF-β-induced EMT enhances the traction forces of A549 cells [63].

To observe the temporal evolution of the traction forces, data were plotted as a kymograph (Fig. 2f). The control group showed a homogeneous pattern along over time, characterized by a dominant red-colored region, indicative of outward traction, at the core. This stable traction pattern with time indicates stable cell-substrate interactions within the monolayer. On the other hand,

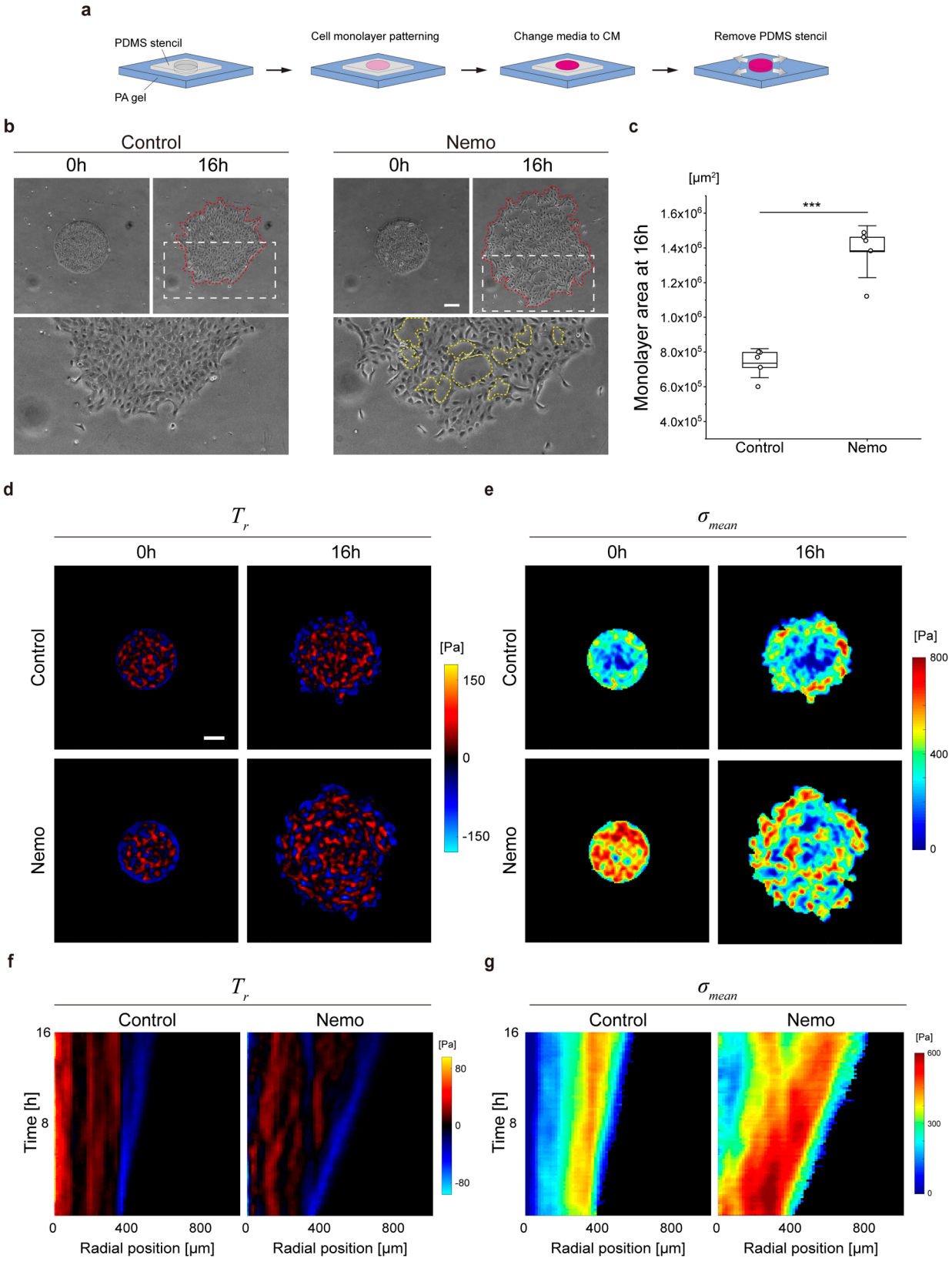

Fig. 2 (See legend on next page.)

(See figure on previous page.)

Fig. 2 Physical analysis of normal breast epithelial cellular monolayer expansion implies the EMT of Nemo-CM-treated cells. (**a**) Schematics of cellular monolayer micropatterning and expansion. (**b**) Phase-contrast images of normal breast epithelial cellular monolayers at 0 and 16 h. Red dotted lines indicate the measured monolayer area at 16 h, while yellow dotted lines represent areas of loss of cell-cell interactions (not included in the area quantification). (**c**) Monolayer area at 16 h. Data represent mean ± SD. $n = 5$ individual monolayers. (**d**) Color-coded maps of radial components of traction (red: outward traction, blue: inward traction). (**e**) Average normal intercellular stress maps. (**f**) Kymographs of radial traction. (**g**) Kymographs of average intercellular stress within the monolayer. Scale bars represent 200 μm. Statistical significance is denoted as follows: $p < 0.001$ (***)

the Nemo-CM-treated group (Nemo group) featured heterogeneous traction patterns. Intercellular stresses were then calculated from the tractions, and the average normal stresses (σ_{mean}) were plotted (Fig. 2e). Right after the free expansion was initiated (at 0 h), the control group displayed low-stress values in general and the lowest in the core of the monolayer. In contrast, the Nemo group exhibited higher stress magnitudes predominantly within the monolayer compared to the control. After 16 h, the control group showed mostly blue spots in the center of the bulk but red spots (high tension) along the edge, which is the tension build-up by the expanding edge. However, the Nemo group showed high-tension regions at both the expanding edge and at the center of the monolayer. The observation suggests that the actively moving outward cells are predominant populations around the monolayer, inducing high tension through the cell-cell junctions. The same trend can be inferred from the average normal stress with time evolution by kymograph (Fig. 2g). The control group maintained low tension at the center, which indicates the tension by the expanding edge was not high enough to transmit to the core of the monolayer. On the other hand, the Nemo group showed high tension in most of the radial positions, and the tension near the expanding edge maintained its magnitude for a relatively long time compared to the center region. Even after 8 h of expansion, the central tension of the Nemo group was higher than control. This observation on monolayers suggests the control and Nemo groups are significantly in different physical states by the influence of the Nemo-CM.

Single cell-based alterations in morphology and migratory behavior support the EMT of normal breast epithelial cells via Nemo-CM

From the cellular monolayer analysis, we observed the disruption of cell-cell interactions and aggressive expansion patterns in the Nemo-CM-treated cellular monolayers, implying the cells underwent EMT. To further investigate the phenotypic transition, we quantified the morphological and migratory features of single cells from MCF10A with different CM conditions. An elongated, spindle-like shape is a key characteristic of mesenchymal cells, reflecting their enhanced migratory capabilities and often caused by alterations in gene expression [8]. Accordingly, changes in shape descriptors such as aspect ratio and circularity can effectively capture this shift toward a mesenchymal-like phenotype [64–69]. The phase-contrast images show representative single MCF10A cells of each CM condition, and we evaluated four morphological features (Fig. 3a). The cell spreading area of each condition showed no difference. However, aspect ratio, circularity, and solidity of cells showed significant differences. These significant differences in the three shape descriptors reflect an elongated, mesenchymal-like morphology implying enhanced migratory capacity in Nemo-CM treated cells. Therefore, we also quantified the migratory ability of single cells.

The trajectories of cells under each CM were plotted, and it was obvious that single cells of the Nemo group migrated more actively than the control (Fig. 3b and Supplementary Video 2). Mean-squared displacement (MSD) was also plotted as a function of time lag. It confirmed again that the Nemo group acquired a migratory phenotype (Fig. 3c). The instantaneous speed of single cells also supported the phenotypic transition of the Nemo group, which indicates the actively migrating characteristics of the cells (Fig. 3d). Additionally, the directionality ratio, indicating the persistence of cell migration, was also higher in the Nemo group than in control (Fig. 3e).

Collectively, the analysis of morphological and migratory features of single cells pointed out the significant phenotypic transition of cells treated with Nemo-CM. This significant shift in both morphology and motility strongly supports our speculation that the Nemo-CM is inducing an EMT in these cells.

Biomolecular assay suggests the *SNAI1*-dependent EMT of normal breast epithelial cells in response to the Nemo-CM

To further verify whether the phenotypic transition via the Nemo-CM is the EMT, we checked the mRNA expression levels of the EMT markers (*CDH1*, *CDH2*, *VIM*) and transcription factors (*SNAI1*, *SNAI2*, *TWIST*, *ZEB1*, *ZEB2*) (Fig. 4a and Supplementary Fig. 1). Only the mRNA expression level of *SNAI1* (Snail) was significantly upregulated in the Nemo group, suggesting that the EMT via Nemo-CM is likely driven by the upregulation of the transcription factor *SNAI1* (Fig. 4a).

Although no significant differences were observed in the mRNA expression levels of *VIM* between the control and Nemo groups, we further investigated vimentin expression at the protein level. Immunofluorescence assays (Fig. 4b–c) and Western blot analyses (Fig. 5) both confirmed that vimentin protein is notably higher

in Nemo-CM–treated cells than in controls. This aligns with our prior identification of the enhanced migratory ability in the Nemo group (Fig. 3b–e), suggesting a more pronounced mesenchymal-like state. Indeed, when epithelial cells like MCF10A are cultured under sparse conditions or otherwise restricted from forming a continuous monolayer, they can induce or upregulate vimentin. However, vimentin expression in Nemo-CM–treated cells was still markedly more intense than that in controls, indicating a stronger pro-EMT influence under Nemo conditions.

By contrast, while *SNAI1* mRNA was significantly upregulated (Fig. 4b), Western blot analysis of SNAIL protein (Fig. 5) showed no marked difference between Control and Nemo samples. This discrepancy may reflect post-transcriptional or post-translational mechanisms that regulate SNAIL stability or timing of expression, highlighting the complexity of EMT regulation.

In summary, these findings collectively suggest that the Nemo-CM induces EMT primarily through the upregulation of transcription factor *SNAI1*, leading to increased vimentin expression and enhanced migratory capabilities in breast epithelial cells.

By integrating mRNA-level measurements (e.g., *SNAI1* upregulation), protein-level validation (enhanced vimentin), and functional assays (monolayer expansion, traction forces, and single-cell morphology/motility), we confirmed that Nemo-CM treatment shifts MCF10A cells toward a more mesenchymal-like state. These multilevel analyses collectively establish that *COX2*$^+$ fibroblast-derived signals induce EMT along both molecular and biophysical dimensions, providing a robust basis for investigating the downstream pathways involved.

The inhibition of EP4 suggests the PGE2-EP4-*SNAI1* axis of the EMT

The effects of PGE2 are transduced via the E series of prostaglandin receptors (EP1, EP2, EP3, and EP4). PGE2 can bind any of these four receptors, and each receptor is coupled to different signaling pathways [70]. Among these EP receptors, EP4 has received attention as a promising therapeutic target in aggressive breast cancers [70, 71]. Western blot analysis confirmed that EP4 protein expression was significantly upregulated in MCF10A cells exposed to Nemo-CM or to control media supplemented with exogenous PGE2, compared to control conditions (Fig. 5). This suggests that PGE2 alone can upregulate EP4 and vimentin in a manner consistent with the EMT phenotype observed under Nemo-CM treatment. Given the observed upregulation of EP4 in response to Nemo-CM, we next evaluated whether Nemo-CM–driven EMT is mediated specifically through EP4 by selectively inhibiting EP4 with L-161,982 (10 μM, dissolved in DMSO) for one hour prior to Nemo-CM treatment.

Consistent with our earlier monolayer expansion observations, the DMSO-treated (vehicle) group exposed to Nemo-CM exhibited pronounced cell-cell junction disruption and an EMT-like phenotype (Fig. 6a and Supplementary Video 3). By contrast, EP4 antagonism prior to Nemo-CM treatment preserved much of the monolayer architecture, reducing the number of disseminating cells and maintaining more stable cell-cell interactions (Fig. 6a), even though the expansion speed of monolayers was not significantly different (Fig. 6b). To further substantiate the partial EMT blockade, we analyzed changes in single-cell morphology and migratory behavior. Our data indicate that the EP4 inhibitor condition exhibits an intermediate morphological state relative to the Control and the Nemo-CM–treated groups. Specifically, although the inhibitor-treated cells show a higher mean aspect ratio compared to the Nemo-CM group, their circularity and solidity shift closer to Control-like values (Fig. 6c). One plausible explanation is cell-to-cell heterogeneity: a subset of inhibitor-treated cells may adopt an elongated but less protrusive shape (thus increasing the aspect ratio), while others revert to a more epithelial morphology, which collectively leads to higher average circularity and solidity. In contrast, the Nemo-CM–treated cells consistently exhibit the most pronounced EMT-like features among the conditions, as indicated by their more irregular and ruffled cell outlines. A similar intermediate phenotype emerges in the migratory data, where inhibitor-treated cells move more than Control but lack the strongly directed motility of Nemo-CM-exposed cells (Fig. 6d). Notably, while Nemo-CM–treated cells display highly directed, persistent motility, inhibitor-treated cells exhibit less directional movement, suggesting a partial suppression of the pro-migratory effects induced by *COX2*$^+$ fibroblast signaling. These findings indicate that although EP4 inhibition attenuates Nemo-CM-induced migratory phenotypes, it does not completely restore control-like motility patterns.

Taken together, these findings demonstrate that EP4 inhibition confers a partial restoration of epithelial characteristics in MCF10A cells exposed to Nemo-CM. While the inhibitor-treated cells still exhibit some signs of mesenchymal-like elongation, their overall shape metrics (circularity, solidity) and migratory patterns represent an intermediate phenotype between control cells and those fully exposed to Nemo-CM. This partial phenotypic rescue, combined with our supplemental Western blot data showing PGE2-induced upregulation of EP4 and vimentin, supports the notion that PGE2–EP4 signaling is a key driver of the EMT program triggered by *COX2*$^+$ fibroblasts, potentially involving a PGE2–EP4–*SNAI1* axis—analogous to the PGE2–EP2–*SNAI1* pathway reported by Cheng et al. [72]. Nevertheless, the incomplete reversal observed with EP4 blockade suggests that additional

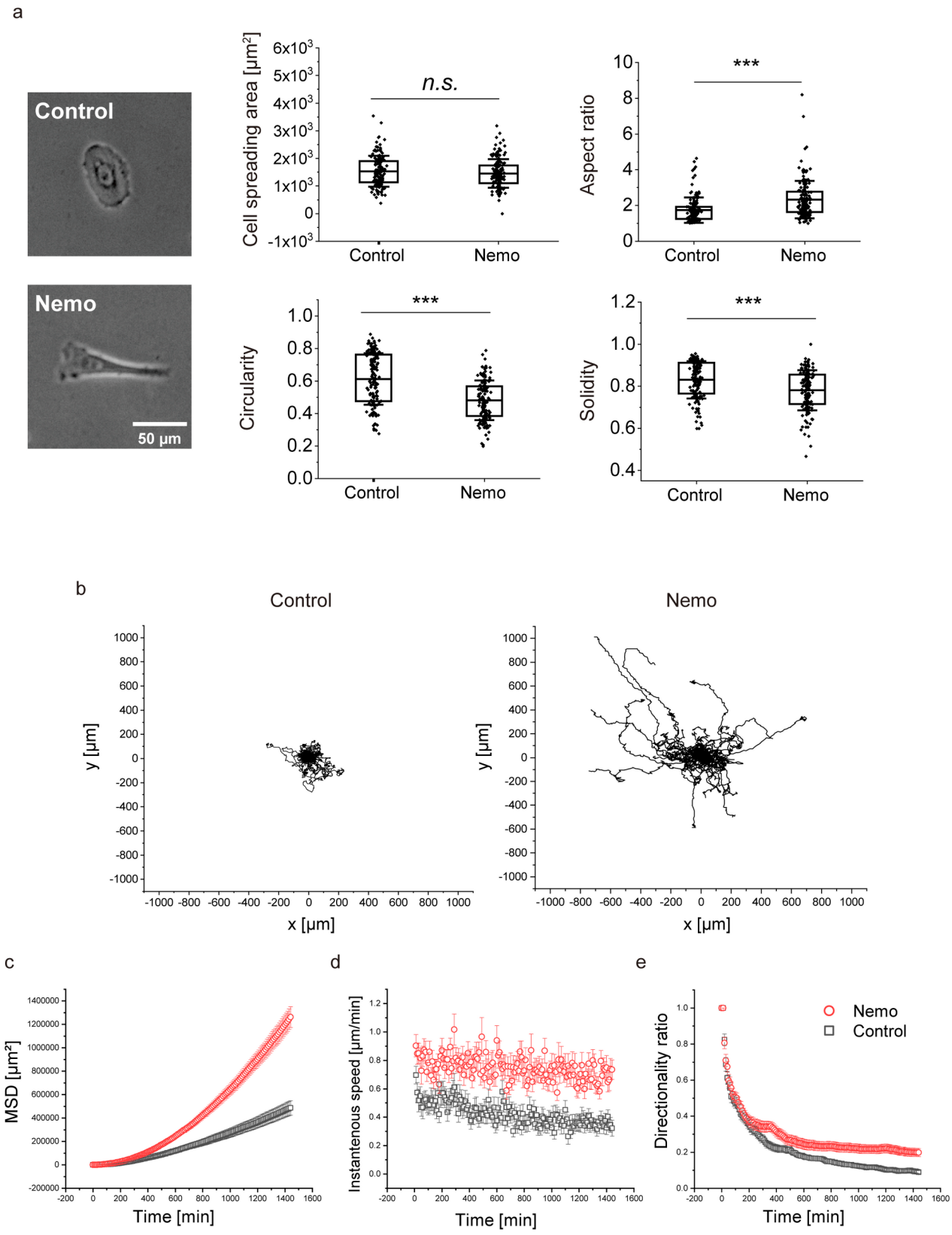

Fig. 3 (See legend on next page.)

(See figure on previous page.)

Fig. 3 Single cell-based alterations in morphology and migratory behavior support the EMT of Nemo-CM-treated group. (**a**) Representative phase-contrast images of single cells under different CM conditions and morphological features. $n = 139$, 149 for control and Nemo, respectively, and the box plot represents mean ± SD. (**b**) Trajectory of single cells in each CM. (**c**) Mean square displacement (MSD) of single cells in each CM. (**d**) Instantaneous speed of single cells in each CM. (**e**) Directionality ratio of single cells in each CM. $n = 60$ cells for each control and Nemo, from three independent experiments respectively (b-e), and data represent mean ± SEM (c-e). Statistical significance is denoted as follows: $p < 0.001$ (***)

factors may also contribute to the full mesenchymal transition in this system.

Discussion

Recent findings highlighted the high *COX2* expression in the TME of various cancer types. The elevated stromal *COX2* expression has been strongly correlated with a poor prognosis in several cancers, including breast cancer. While the tumor stroma is composed of diverse cell types, there is growing evidence that *COX2* is expressed by some CAFs, known for their role in immunosuppression within tumors [27, 73–76]. This suggests that *COX2*$^+$ CAFs may significantly contribute to the overall *COX2* expression in the stroma. If we can decouple the *COX2*$^+$ CAFs and other cells in TME, we could illuminate their unique impact on tumor progression.

Leveraging the process of nemosis to induce a state analogous to *COX2*$^+$ CAFs in vitro, our study explored the paracrine influences of *COX2*$^+$ CAFs on breast cancer progression. The paracrine signaling of *COX2*$^+$ CAFs was simulated using conditioned media. We demonstrated that the conditioned media from *COX2*$^+$ fibroblasts (the proxy of *COX2*$^+$ CAFs) induced the EMT of normal breast epithelial cells, validated through both cell mechanics-based analyses and biomolecular assays. These comprehensive investigations—spanning monolayer expansion studies, quantification of single-cell biophysical attributes, and multi-level EMT marker evaluations (transcriptional and protein) —converge to substantiate the EMT induction by Nemo-CM.

To further test the generalizability of *COX2*$^+$ fibroblast-driven EMT, we isolated primary fibroblasts from breast tissue and confirmed nemosis induction via significantly elevated *COX2* mRNA expression (Supplementary Fig. 2). We then treated both MCF10A and MCF-7 cells with conditioned media from these primary fibroblasts (Control-CM vs. Nemo-CM) (Supplementary Figs. 2–4). In MCF10A cells, exposure to primary Nemo-CM led to a marked upregulation of *SNAI2* (Slug)—whereas our original HDF–MCF10A model predominantly showed *SNAI1* (Snail). Alongside this shift in transcription factor usage, the MCF10A monolayers treated with primary Nemo-CM exhibited EMT-like alterations, including accelerated expansion and loss of stable cell-cell interactions. Although only a trend toward increased vimentin protein levels was noted (not reaching statistical significance), the collective results—morphological changes, significant *SNAI2* induction, and disrupted cell-cell contacts—demonstrate that primary Nemo-CM effectively triggers an EMT-like response in MCF10A.

By contrast, MCF-7 cells treated with the same primary Nemo-CM displayed robust *ZEB1* mRNA upregulation but no appreciable differences in vimentin protein or monolayer expansion, indicating only a partial EMT response. These findings are consistent with prior literature showing that non-tumorigenic MCF10A cells possess greater epithelial plasticity and more readily undergo EMT in response to external stimuli such as TGF-β1 or fibroblast-conditioned media. In contrast, MCF-7 cells, which are luminal and tumor-derived, often exhibit attenuated EMT responses that are confined to transcriptional changes [77]. This context-dependent variability may be influenced by baseline signaling networks or inherent transcriptional regulatory differences among various epithelial cell lines. This context-dependent variability may be influenced by baseline signaling networks or inherent transcriptional regulatory differences among various epithelial cell lines.

To probe the underlying mechanism, we examined the role of the PGE2–EP4 signaling axis as a mediator of *COX2*$^+$ fibroblast-induced phenotypic changes (Fig. 7). While both EP2 and EP4 activate cAMP/PKA signaling, EP4 uniquely engages additional pathways, including PI3K/Akt, ERK, and β-catenin—key regulators of EMT, cell survival, and migration [71]. This broader signaling capacity distinguishes EP4 as a dominant mediator of PGE2-driven tumor progression, particularly in breast cancer [70, 71], making it the focus of our investigation.

Consistent with this, our experimental data demonstrate that EP4 inhibition preserved cell-cell interactions and limited monolayer expansion (Fig. 6), suggesting that EP4 signaling promotes the loss of epithelial cohesion—a key early event in EMT. Additionally, single-cell morphological and migratory analyses revealed a partial rescue of the mesenchymal-like phenotype under EP4 inhibition, with the inhibitor-treated samples displaying an intermediate phenotype between Nemo-CM and Control (Fig. 6c–d). This nuanced result underscores EP4's major contribution to Nemo-induced EMT, while suggesting that additional factors may sustain the full mesenchymal transition.

Having established that EP4 inhibition partially restores epithelial-like characteristics at the cellular level, we next considered the molecular mechanisms that may underlie these phenotypic changes. Our study demonstrated that *SNAI1* mRNA levels were significantly upregulated in

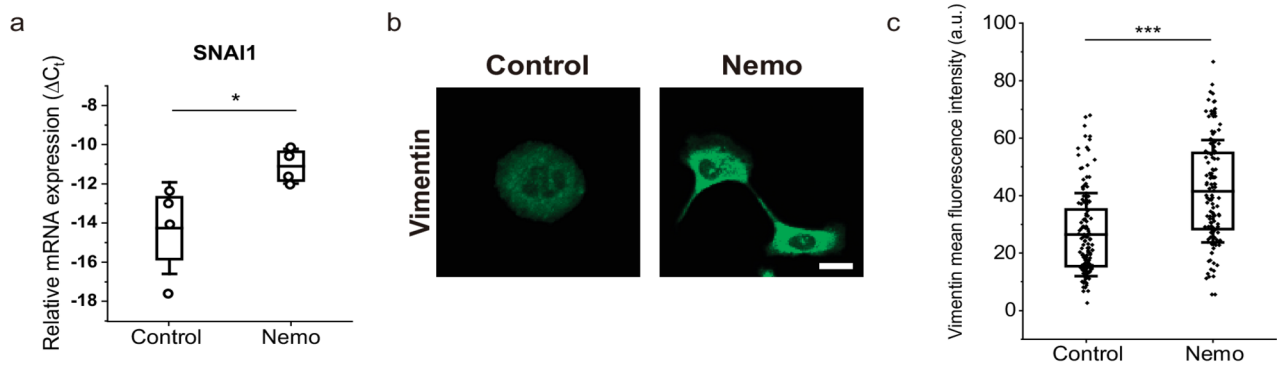

Fig. 4 Biomolecular assay suggests the EMT of normal breast epithelial cells via Nemo-CM. (**a**) mRNA expression of EMT transcription factors *SNAI1*. $n = 4$ and data represent mean ± SEM. (**b**) Vimentin characterization by immunofluorescence of representative images. Scale bar: 20 µm (**c**) Quantification of mean intensity of vimentin. $n = 141$, 131 for control and Nemo respectively, and the box plot represents mean ± SD. Statistical significance is denoted as follows: $p < 0.05$ (*), $p < 0.001$ (***)

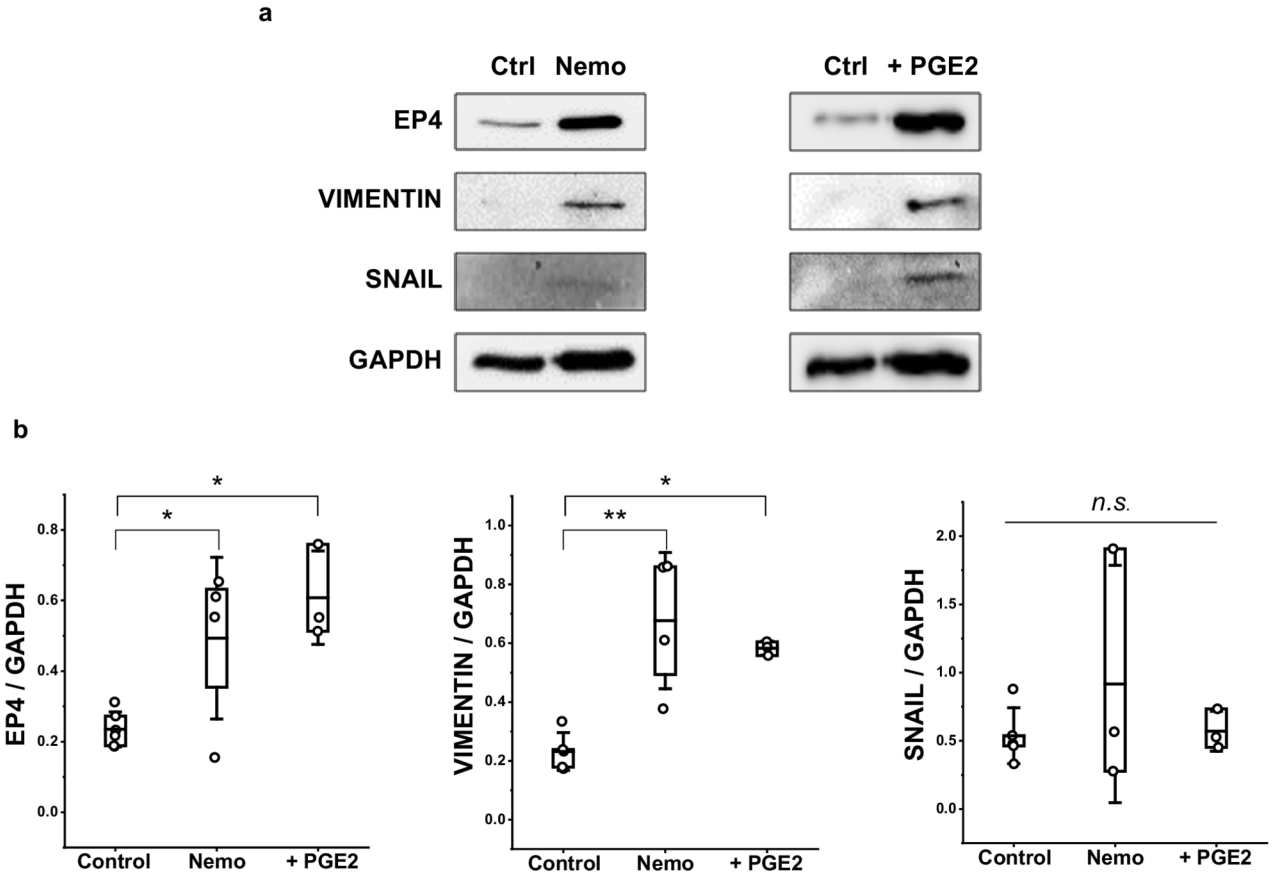

Fig. 5 EP4 and EMT marker expression in MCF10A cells treated with Nemo-CM or exogenous PGE2. (**a**) Representative Western blot images showing EP4, Vimentin, and SNAIL protein levels in MCF10A cells treated with conditioned media from control fibroblasts (Control), nemosis-induced fibroblasts (Nemo), or Control-CM supplemented with PGE2 (+PGE2; 3,000 pg/ml). GAPDH was used as a loading control. Blots for each condition were run and imaged separately. (**b**) Box plots showing densitometric quantification of protein expression levels for EP4, Vimentin, and SNAIL, normalized to GAPDH (Protein/GAPDH). Data were pooled from independent biological replicates: Control ($n = 6$ for EP4; $n = 5$ for VIMENTIN and SNAIL), Nemo ($n = 4$), Control + PGE2 ($n = 3$). Statistical comparisons were performed using one-way ANOVA with post hoc testing. Statistical significance is denoted as follows: $p < 0.05$ (*), $p < 0.01$ (**)

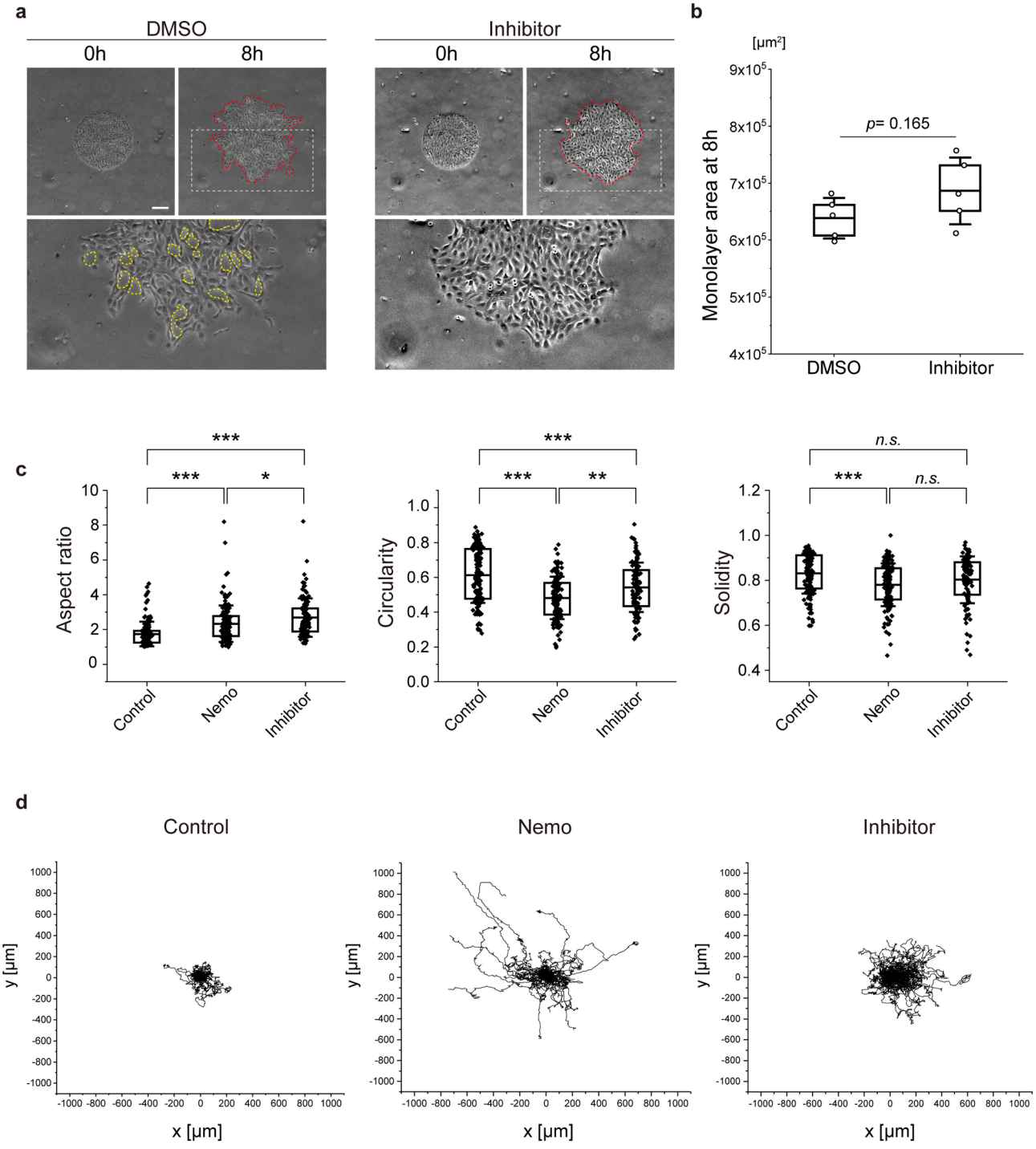

Fig. 6 The EP4 inhibition preserves the cell-cell interactions in cellular monolayers and supports the role of the PGE2-EP4-SNAI1 signaling axis in EMT. (**a**) Phase-contrast images of normal breast epithelial cellular monolayers without (DMSO only) and with PGE2 inhibitor at 0 and 8 h. Red dotted lines indicate the measured monolayer area at 8 h, while yellow dotted lines represent regions of loss of cell-cell interactions (not included in the area quantification). (**b**) Monolayer area at 8 h. Data represent mean ± SD. $n = 5$ individual monolayers. The scale bar represents 200 μm. (**c**) Single-cell morphology parameters: aspect ratio, circularity, and solidity. For Control, $n = 139$ cells; for Nemo, $n = 149$; and for inhibitor-treated samples, $n = 111$. Data are presented as mean ± SD. (**d**) Trajectory of single cells in each control CM, Nemo CM, and Nemo CM with EP4 inhibitor. $n = 60, 60, 56$ cells for each control, Nemo, and Nemo with EP4 inhibitor from three independent experiments respectively. Control and Nemo data in (**c-d**) are re-presented from Fig. 3 to facilitate direct comparison with the newly added Inhibitor data. Statistical significance is denoted as follows: $p < 0.05$ (*), $p < 0.01$ (**), $p < 0.001$ (***)

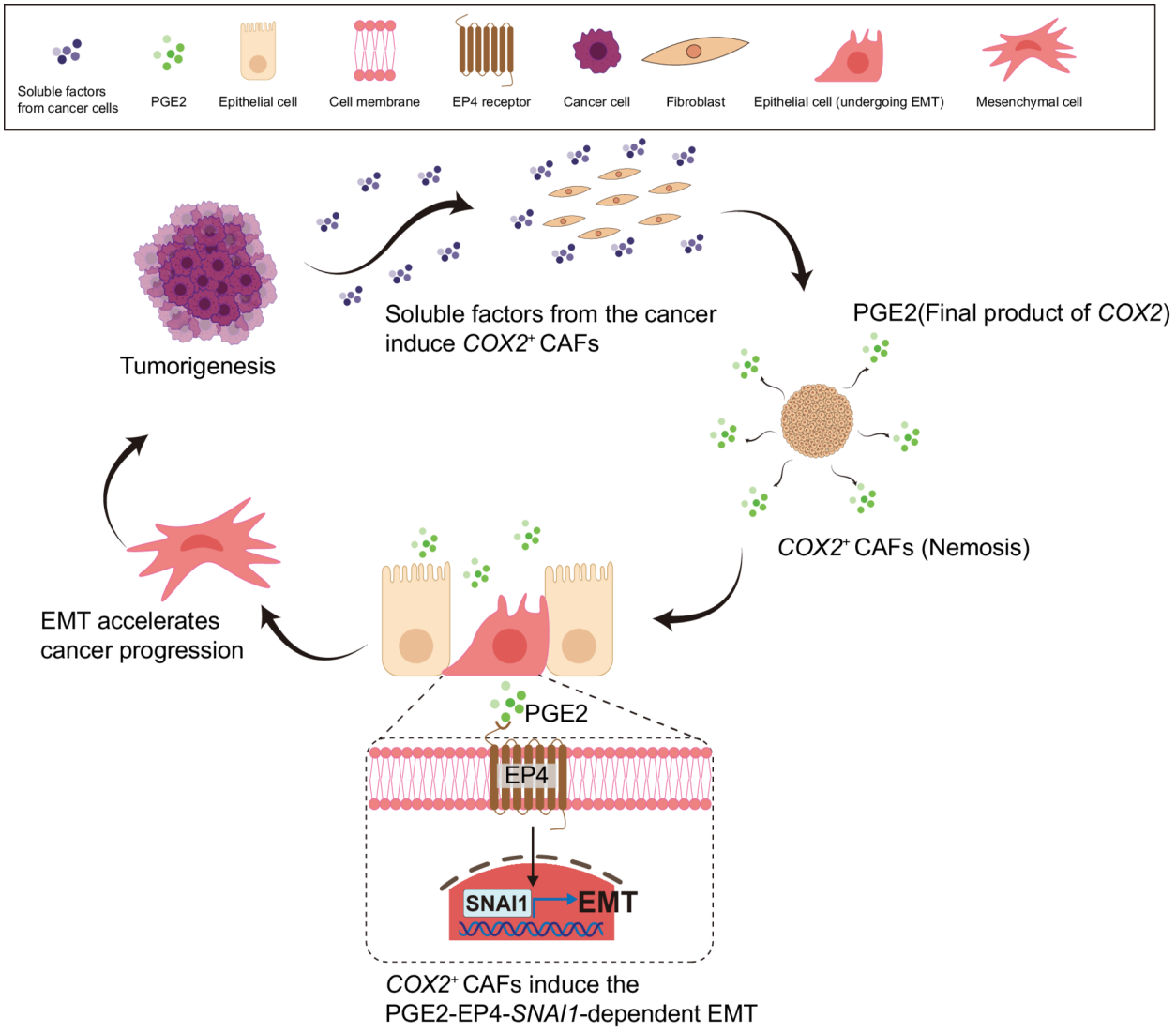

Fig. 7 Illustration of the newly proposed feedback mechanism in breast cancer mediated by *COX2*$^+$ CAF via the PGE2-EP4-*SNAI1* axis

response to Nemo-CM, consistent with its role as a key transcriptional regulator of EMT. While the direct link between EP4 and *SNAI1* remains to be fully elucidated, previous studies have shown that EP4 activation engages multiple intracellular pathways, including cAMP/PKA, PI3K/Akt, and MAPK/ERK, all of which have been implicated in EMT progression [70–72, 78]. These pathways are known to regulate key EMT transcription factors, including *SNAI1*, through mechanisms such as enhanced transcriptional activity (via PKA/ERK) or increased protein stability (via Akt). Based on these mechanisms and our experimental findings, we propose the PGE2–EP4–*SNAI1* axis as a putative pathway through which *COX2*$^+$ fibroblasts drive EMT in breast cancer (Fig. 7). Our model integrates these signaling pathways with our observations, providing a framework for future studies to further investigate the molecular regulation of EMT in response to *COX2*$^+$ fibroblast signaling.

Nonetheless, we acknowledge that EP2 may also contribute to PGE2-mediated signaling and that its relative contribution to EMT remains an open question. A direct comparison of EP2 and EP4 inhibition would help determine whether EP2 acts independently in promoting EMT or functions synergistically with EP4. Additionally, assessing phosphorylation states of key signaling molecules or performing promoter analyses of *SNAI1* could clarify whether EP4 directly regulates *SNAI1* transcription or influences its protein stability via intermediary kinases.

While our in vitro study offers detailed insights into the specific role of *COX2*$^+$ CAFs in the tumor microenvironment, it inherently carries some limitations. The controlled conditions of in vitro experiments allow us

to decouple the complex interactions within the tumor microenvironment, providing a clear view of how *COX2*$^+$ CAFs influence neighboring cells. This isolation is crucial for understanding the specific pathways and interactions at play, such as the *COX2*$^+$ CAFs-PGE2-EP4-*SNAI1* axis which we propose based on our findings and prior literature. However, these advantages also introduce constraints. The tumor microenvironment in vivo involves a dynamic interplay of multiple cell types, extracellular matrix components, and a host of soluble factors that cannot be fully replicated in vitro. Our model, focused primarily on the interactions between *COX2*$^+$ fibroblasts and epithelial cells, does not incorporate other cellular components, notably immune cells, which play a significant role in cancer progression and response to therapy. Additionally, the use of conditioned media may not entirely mimic the direct cell-cell and cell-matrix interactions present in vivo.

To address these limitations, future research should extend these findings through in vivo studies or sophisticated 3D culture systems that better emulate the actual tumor stroma. Such studies will help validate the translational relevance of the *COX2*$^+$ CAFs-PGE2-EP4-*SNAI1* axis in clinical settings and potentially guide the development of targeted therapies. Further investigations involving the interplay between *COX2*+CAFs and immune cells could also enrich our understanding of the tumor microenvironment's complexity.

Supplementary Information

The online version contains supplementary material available at https://doi.org/10.1186/s12964-025-02227-7.

Supplementary Fig. 1 mRNA expression of EMT markers (CDH1, CDH2, VIM) and transcription factors (SNAI2, TWIST, ZEB1, ZEB2). n = 4 and data represent mean ± sem.

Supplementary Fig. 2*COX2* induction in primary fibroblasts and EMT gene expression in MCF10A and MCF-7 cells treated with conditioned media from primary fibroblasts. (**a**) Primary fibroblasts were isolated from capsular contracture tissue (Baker grade I) obtained during surgery at Soonchunhyang University Hospital Seoul. The use of human tissue was approved by the Institutional Review Board of KAIST (IRB approval number: KH2022-109), and informed consent was obtained from all patients prior to tissue collection. (**b**) ***COX2*** mRNA expression in primary fibroblasts cultured on flat (96_flat) versus round-bottom (96_round) 96-well plates. Nemosis was induced by aggregate formation in round-bottom wells, resulting in significantly elevated COX2 expression compared to fibroblasts in 2D conditions. n = 3. Statistical significance is denoted as follows: $p < 0.05$ (*).

Supplementary Fig. 3 Primary fibroblast-derived conditioned media recapitulate key EMT-like phenotypes in MCF10A cells. (**a**) Schematic of experimental setup. MCF10A cells were treated with conditioned media (CM) from either control (Ctrl) or nemotic (Nemo) primary fibroblasts (Prim-FB). (**b**) qRT-PCR analysis of EMT-related genes in MCF10A cells treated with conditioned media (CM) from control or nemotic (Nemo) primary fibroblasts. Among the genes tested, ***SNAI2*** showed significant upregulation in the Nemo-CM condition. (**c**) Western blot analysis reveals a trend toward increased vimentin expression in Nemo-CM–treated MCF10A cells; however, the difference between groups did not reach statistical significance. n = 3. (d) Phase-contrast images of MCF10A cellular monolayers at 0 and 16h. Red dotted lines indicate the measured monolayer area at 16h, while yellow dotted lines represent areas of loss of cell-cell interactions (not included in the area quantification). (**d**) Quantification of monolayer area at 16h reveals significant expansion in the Nemo-CM group relative to control. Data represent mean ± SD. n = 7 individual monolayers; scale bar: 200 µm. Statistical significance is denoted as follows: $p < 0.01$ (**).

Supplementary Fig. 4 Conditioned media from nemotic primary fibroblasts induces limited EMT-like responses in MCF-7 cells. (**a**) Schematic of experimental setup. MCF-7 cells were treated with conditioned media (CM) from either control (Ctrl) or nemotic (Nemo) primary fibroblasts (Prim-FB). (**b**) qRT-PCR analysis of EMT-related genes in MCF-7 cells treated with conditioned media (CM) from control or nemotic (Nemo) primary fibroblasts. Among the genes tested, ***ZEB1*** was significantly upregulated ($p < 0.05$); other markers showed no significant change (n.s.). (**c**) Western blot analysis reveals a trend toward increased vimentin expression in Nemo-CM–treated MCF-7 cells; however, the difference between groups did not reach statistical significance. n = 3. (**d**) Phase-contrast images of MCF-7 cellular monolayers at 0 and 16h. Red dotted lines indicate the measured monolayer area at 16h. (**d**) Quantification of monolayer area at 16h indicates no statistically significant difference between groups. Data represent mean ± SD. n = 3 individual monolayers; scale bar: 200 µm.

Supplementary Video 1. Monolayer expansion of MCF10A cells under different conditioned media (CM) conditions. MCF10A monolayers cultured with Nemo-CM expand more rapidly and extensively compared to those treated with Control-CM.

Supplementary Video 2. Representative single-cell migration trajectories of MCF10A cells treated with Control-CM (left) or Nemo-CM (right). Cells exposed to Nemo-CM exhibited more active and persistent migration compared to Control-CM-treated cells. Scale bar: 50 µm.

Supplementary Video 3. Monolayer expansion dynamics of MCF10A cells treated with Nemo-CM, with or without EP4 antagonist. DMSO-treated (vehicle) cells exposed to Nemo-CM exhibit pronounced cell-cell junction disruption and an EMT-like phenotype, while EP4 inhibition partially preserves monolayer integrity and limits cell dissemination.

Author contributions

M.K. and S.D. conceived the research and designed experiments. M.K., S.D., N.J.S. and T.Y.K. performed the experiments. M.K., S.D., and J.H.S. interpreted data. M.K. wrote the manuscript. All authors edited the manuscript.

Funding

This research was supported by the National Research Foundation grant from the Korean government (NRF-2021R1A2C3008408) and the Korean Fund for Regenerative Medicine (KFRM) grant, funded by the Korea government (the Ministry of Science and ICT, the Ministry of Health & Welfare). (22B0401L1)

Data availability

The datasets used and analyzed during the current study are available from the corresponding author upon reasonable request.

Declarations

Ethics approval and consent to participate

N.A.

Consent for publication

N.A.

Competing interests

The authors declare no competing interests.

Author details

[1]Department of Mechanical Engineering, Korea Advanced Institute of Science and Technology, 291 Daehak-Ro, Yuseong-Gu, Daejeon 34141, Republic of Korea
[2]KAIST Institute for Health Science and Technology, Korea Advanced Institute of Science and Technology, 291 Daehak-Ro, Yuseong-Gu, Daejeon 34141, Republic of Korea

[3]Graduate School of Stem Cell and Regenerative Biology, Korea Advanced Institute of Science and Technology, 291 Daehak-Ro, Yuseong-Gu, Daejeon 34141, Republic of Korea

Received: 21 October 2024 / Accepted: 30 April 2025
Published online: 22 May 2025

References

1. Spill F, Reynolds DS, Kamm RD, Zaman MH. Impact of the physical microenvironment on tumor progression and metastasis. Curr Opin Biotechnol. 2016;40:41–8.
2. Ghoshdastider U, Rohatgi N, Mojtabavi Naeini M, Baruah P, Revkov E, Guo YA, et al. Pan-Cancer analysis of Ligand-Receptor Cross-talk in the tumor microenvironment. Cancer Res. 2021;81(7):1802–12.
3. Acerbi I, Cassereau L, Dean I, Shi Q, Au A, Park C, et al. Human breast cancer invasion and aggression correlates with ECM stiffening and immune cell infiltration. Integr Biol (Camb). 2015;7(10):1120–34.
4. Devarasou S, Kang M, Kwon TY, Cho Y, Shin JH. Fibrous matrix Architecture-Dependent activation of fibroblasts with a Cancer-Associated Fibroblast-like phenotype. ACS Biomater Sci Eng. 2023;9(1):280–91.
5. Devarasou S, Kang M, Shin JH. Biophysical perspectives to Understanding cancer-associated fibroblasts. APL Bioeng. 2024;8(2):021507.
6. Zhang H, Yue X, Chen Z, Liu C, Wu W, Zhang N, et al. Define cancer-associated fibroblasts (CAFs) in the tumor microenvironment: new opportunities in cancer immunotherapy and advances in clinical trials. Mol Cancer. 2023;22(1):159.
7. Kalluri R, Weinberg RA. The basics of epithelial-mesenchymal transition. J Clin Invest. 2009;119(6):1420–8.
8. Yang J, Antin P, Berx G, Blanpain C, Brabletz T, Bronner M, et al. Guidelines and definitions for research on epithelial-mesenchymal transition. Nat Rev Mol Cell Biol. 2020;21(6):341–52.
9. Chaffer CL, San Juan BP, Lim E, Weinberg RA. EMT, cell plasticity and metastasis. Cancer Metastasis Rev. 2016;35(4):645–54.
10. Tsai JH, Yang J. Epithelial-mesenchymal plasticity in carcinoma metastasis. Genes Dev. 2013;27(20):2192–206.
11. Tsai JH, Donaher JL, Murphy DA, Chau S, Yang J. Spatiotemporal regulation of epithelial-mesenchymal transition is essential for squamous cell carcinoma metastasis. Cancer Cell. 2012;22(6):725–36.
12. Ocana OH, Corcoles R, Fabra A, Moreno-Bueno G, Acloque H, Vega S, et al. Metastatic colonization requires the repression of the epithelial-mesenchymal transition inducer Prrx1. Cancer Cell. 2012;22(6):709–24.
13. Smith WL, Garavito RM, DeWitt DL. Prostaglandin endoperoxide H synthases (cyclooxygenases)-1 and– 2. J Biol Chem. 1996;271(52):33157–60.
14. Nagao M, Sato Y, Yamauchi A. A meta-analysis of PTGS1 and PTGS2 polymorphisms and NSAID intake on the risk of developing cancer. PLoS ONE. 2013;8(8):e71126.
15. Raj V, Bhadauria AS, Singh AK, Kumar U, Rai A, Keshari AK, et al. Novel 1,3,4-thiadiazoles inhibit colorectal cancer via Blockade of IL-6/COX-2 mediated JAK2/STAT3 signals as evidenced through data-based mathematical modeling. Cytokine. 2019;118:144–59.
16. Gurram B, Zhang S, Li M, Li H, Xie Y, Cui H, et al. Celecoxib conjugated fluorescent probe for identification and discrimination of Cyclooxygenase-2 enzyme in Cancer cells. Anal Chem. 2018;90(8):5187–93.
17. Hashemi Goradel N, Najafi M, Salehi E, Farhood B, Mortezaee K. Cyclooxygenase-2 in cancer: A review. J Cell Physiol. 2019;234(5):5683–99.
18. Sun H, Zhang X, Sun D, Jia X, Xu L, Qiao Y, et al. COX-2 expression in ovarian cancer: an updated meta-analysis. Oncotarget. 2017;8(50):88152–62.
19. Sharma S, Yang SC, Zhu L, Reckamp K, Gardner B, Baratelli F, et al. Tumor cyclooxygenase-2/prostaglandin E2-dependent promotion of FOXP3 expression and CD4 + CD25 + T regulatory cell activities in lung cancer. Cancer Res. 2005;65(12):5211–20.
20. Montezuma MAP, Fonseca FP, Benites BM, Soares CD, do, Amaral-Silva GK, de Almeida OP et al. COX-2 as a determinant of lower disease-free survival for patients affected by ameloblastoma. Pathol Res Pract. 2018;214(6):907– 13.
21. Hoing B, Kanaan O, Altenhoff P, Petri R, Thangavelu K, Schluter A, et al. Stromal versus tumoral inflammation differentially contribute to metastasis and poor survival in laryngeal squamous cell carcinoma. Oncotarget. 2018;9(9):8415–26.
22. Hung JH, Su IJ, Lei HY, Wang HC, Lin WC, Chang WT, et al. Endoplasmic reticulum stress stimulates the expression of cyclooxygenase-2 through activation of NF-kappaB and pp38 mitogen-activated protein kinase. J Biol Chem. 2004;279(45):46384–92.
23. Zhou TJ, Zhang SL, He CY, Zhuang QY, Han PY, Jiang SW, et al. Downregulation of mitochondrial cyclooxygenase-2 inhibits the stemness of nasopharyngeal carcinoma by decreasing the activity of dynamin-related protein 1. Theranostics. 2017;7(5):1389–406.
24. Huang H, Aladelokun O, Ideta T, Giardina C, Ellis LM, Rosenberg DW. Inhibition of PGE2/EP4 receptor signaling enhances oxaliplatin efficacy in resistant colon cancer cells through modulation of oxidative stress. Sci Rep. 2019;9(1):4954.
25. Esbona K, Inman D, Saha S, Jeffery J, Schedin P, Wilke L, et al. COX-2 modulates mammary tumor progression in response to collagen density. Breast Cancer Res. 2016;18(1):35.
26. Roulis M, Kaklamanos A, Schernthanner M, Bielecki P, Zhao J, Kaffe E, et al. Paracrine orchestration of intestinal tumorigenesis by a mesenchymal niche. Nature. 2020;580(7804):524–9.
27. Zhu Y, Shi C, Zeng L, Liu G, Jiang W, Zhang X, et al. High COX-2 expression in cancer-associated fibiroblasts contributes to poor survival and promotes migration and invasiveness in nasopharyngeal carcinoma. Mol Carcinog. 2020;59(3):265–80.
28. Su CW, Zhang Y, Zhu YT. Stromal COX-2 signaling are correlated with colorectal cancer: A review. Crit Rev Oncol Hematol. 2016;107:33–8.
29. Krishnamachary B, Stasinopoulos I, Kakkad S, Penet MF, Jacob D, Wildes F, et al. Breast cancer cell cyclooxygenase-2 expression alters extracellular matrix structure and function and numbers of cancer associated fibroblasts. Oncotarget. 2017;8(11):17981–94.
30. Zhu M, Zhu Y, Lance P. TNFalpha-activated stromal COX-2 signalling promotes proliferative and invasive potential of colon cancer epithelial cells. Cell Prolif. 2013;46(4):374–81.
31. Zhu Y, Zhu M, Lance P. IL1beta-mediated stromal COX-2 signaling mediates proliferation and invasiveness of colonic epithelial cancer cells. Exp Cell Res. 2012;318(19):2520–30.
32. Majumder M, Dunn L, Liu L, Hasan A, Vincent K, Brackstone M, et al. COX-2 induces oncogenic micro RNA miR655 in human breast cancer. Sci Rep. 2018;8(1):327.
33. Ramu A, Kathiresan S, Ramadoss H, Nallu A, Kaliyan R, Azamuthu T. Gramine attenuates EGFR-mediated inflammation and cell proliferation in oral carcinogenesis via regulation of NF-kappa B and STAT3 signaling. Biomed Pharmacother. 2018;98:523–30.
34. Todoric J, Antonucci L, Karin M. Targeting inflammation in Cancer prevention and therapy. Cancer Prev Res (Phila). 2016;9(12):895–905.
35. Hosseini F, Mahdian-Shakib A, Jadidi-Niaragh F, Enderami SE, Mohammadi H, Hemmatzadeh M, et al. Anti-inflammatory and anti-tumor effects of alpha-l-guluronic acid (G2013) on cancer-related inflammation in a murine breast cancer model. Biomed Pharmacother. 2018;98:793–800.
36. Kim S, Campbell J, Yoo W, Taylor JA, Sandler DP. Systemic levels of estrogens and PGE2 synthesis in relation to postmenopausal breast Cancer risk. Cancer Epidemiol Biomarkers Prev. 2017;26(3):383–8.
37. Yip-Schneider MT, Carr RA, Wu H, Schmidt CM. Prostaglandin E2: A pancreatic fluid biomarker of intraductal papillary mucinous neoplasm dysplasia. J Am Coll Surg. 2017;225(4):481–7.
38. Lai YH, Liu H, Chiang WF, Chen TW, Chu LJ, Yu JS, et al. MiR-31-5p-ACOX1 Axis enhances tumorigenic fitness in oral squamous cell carcinoma via the promigratory prostaglandin E2. Theranostics. 2018;8(2):486–504.
39. Finetti F, Travelli C, Ercoli J, Colombo G, Buoso E, Trabalzini L. Prostaglandin E2 and cancer: insight into tumor progression and immunity. Biology (Basel). 2020;9(12).
40. Zhang A, Wang MH, Dong Z, Yang T. Prostaglandin E2 is a potent inhibitor of epithelial-to-mesenchymal transition: interaction with hepatocyte growth factor. Am J Physiol Ren Physiol. 2006;291(6):F1323–31.
41. Vaheri A, Enzerink A, Rasanen K, Salmenpera P. Nemosis, a novel way of fibroblast activation, in inflammation and cancer. Exp Cell Res. 2009;315(10):1633–8.
42. Kankuri E, Cholujova D, Comajova M, Vaheri A, Bizik J. Induction of hepatocyte growth factor/scatter factor by fibroblast clustering directly promotes tumor cell invasiveness. Cancer Res. 2005;65(21):9914–22.
43. Dror S, Sander L, Schwartz H, Sheinboim D, Barzilai A, Dishon Y, et al. Melanoma MiRNA trafficking controls tumour primary niche formation. Nat Cell Biol. 2016;18(9):1006–17.
44. Haass NK, Smalley KS, Li L, Herlyn M. Adhesion, migration and communication in melanocytes and melanoma. Pigment Cell Res. 2005;18(3):150–9.

45. Ruiter D, Bogenrieder T, Elder D, Herlyn M. Melanoma-stroma interactions: structural and functional aspects. Lancet Oncol. 2002;3(1):35–43.
46. Duda DG, Duyverman AM, Kohno M, Snuderl M, Steller EJ, Fukumura D, et al. Malignant cells facilitate lung metastasis by bringing their own soil. Proc Natl Acad Sci U S A. 2010;107(50):21677–82.
47. Ao Z, Shah SH, Machlin LM, Parajuli R, Miller PC, Rawal S, et al. Identification of Cancer-Associated fibroblasts in Circulating blood from patients with metastatic breast Cancer. Cancer Res. 2015;75(22):4681–7.
48. Rasanen K, Virtanen I, Salmenpera P, Grenman R, Vaheri A. Differences in the nemosis response of normal and cancer-associated fibroblasts from patients with oral squamous cell carcinoma. PLoS ONE. 2009;4(9):e6879.
49. Bizik J, Kankuri E, Ristimaki A, Taieb A, Vapaatalo H, Lubitz W, et al. Cell-cell contacts trigger programmed necrosis and induce cyclooxygenase-2 expression. Cell Death Differ. 2004;11(2):183–95.
50. Jang H, Kim J, Shin JH, Fredberg JJ, Park CY, Park Y. Traction microscopy integrated with microfluidics for chemotactic collective migration. J Vis Exp. 2019(152).
51. Butler JP, Tolic-Norrelykke IM, Fabry B, Fredberg JJ. Traction fields, moments, and strain energy that cells exert on their surroundings. Am J Physiol Cell Physiol. 2002;282(3):C595–605.
52. Trepat X, Wasserman MR, Angelini TE, Millet E, Weitz DA, Butler JP, et al. Physical forces during collective cell migration. Nat Phys. 2009;5(6):426–30.
53. Notbohm J, Banerjee S, Utuje KJC, Gweon B, Jang H, Park Y, et al. Cellular contraction and polarization drive collective cellular motion. Biophys J. 2016;110(12):2729–38.
54. Tambe DT, Hardin CC, Angelini TE, Rajendran K, Park CY, Serra-Picamal X, et al. Collective cell guidance by cooperative intercellular forces. Nat Mater. 2011;10(6):469–75.
55. Tambe DT, Croutelle U, Trepat X, Park CY, Kim JH, Millet E et al. Monolayer stress microscopy: limitations, artifacts, and accuracy of recovered intercellular stresses. PLoS ONE. 2013;8(2).
56. Schneider CA, Rasband WS, Eliceiri KW. NIH image to imageJ: 25 years of image analysis. Nat Methods. 2012;9(7):671–5.
57. Konishi H, Mohseni M, Tamaki A, Garay JP, Croessmann S, Karnan S, et al. Mutation of a single allele of the cancer susceptibility gene BRCA1 leads to genomic instability in human breast epithelial cells. Proc Natl Acad Sci U S A. 2011;108(43):17773–8.
58. Weiss MB, Vitolo MI, Mohseni M, Rosen DM, Denmeade SR, Park BH, et al. Deletion of p53 in human mammary epithelial cells causes chromosomal instability and altered therapeutic response. Oncogene. 2010;29(33):4715–24.
59. Vitolo MI, Weiss MB, Szmacinski M, Tahir K, Waldman T, Park BH, et al. Deletion of PTEN promotes tumorigenic signaling, resistance to Anoikis, and altered response to chemotherapeutic agents in human mammary epithelial cells. Cancer Res. 2009;69(21):8275–83.
60. Kwon TY, Jeong J, Park E, Cho Y, Lim D, Ko UH, et al. Physical analysis reveals distinct responses of human bronchial epithelial cells to guanidine and Isothiazolinone biocides. Toxicol Appl Pharmacol. 2021;424:115589.
61. Sutton AA, Molter CW, Amini A, Idicula J, Furman M, Tirgar P, et al. Cell monolayer deformation microscopy reveals mechanical fragility of cell monolayers following EMT. Biophys J. 2022;121(4):629–43.
62. Yoshie H, Koushki N, Molter C, Siegel PM, Krishnan R, Ehrlicher AJ. High throughput traction force microscopy using PDMS reveals Dose-Dependent effects of transforming growth Factor-beta on the Epithelial-to-Mesenchymal transition. J Vis Exp. 2019;(148).
63. Biondini M, Duclos G, Meyer-Schaller N, Silberzan P, Camonis J, Parrini MC. RalB regulates contractility-driven cancer dissemination upon TGFbeta stimulation via the RhoGEF GEF-H1. Sci Rep. 2015;5:11759.
64. Isert L, Mehta A, Loiudice G, Oliva A, Roidl A, Merkel OM. An in vitro approach to model EMT in breast Cancer. Int J Mol Sci. 2023;24(9).
65. Leggett SE, Sim JY, Rubins JE, Neronha ZJ, Williams EK, Wong IY. Morphological single cell profiling of the epithelial-mesenchymal transition. Integr Biol (Camb). 2016;8(11):1133–44.
66. Nurmagambetova A, Mustyatsa V, Saidova A, Vorobjev I. Morphological and cytoskeleton changes in cells after EMT. Sci Rep. 2023;13(1):22164.
67. Ren ZX, Yu HB, Li JS, Shen JL, Du WS. Suitable parameter choice on quantitative morphology of A549 cell in epithelial-mesenchymal transition. Biosci Rep. 2015;35(3).
68. Sarkar A, Barui A, Sengupta S, Chatterjee J, Ghorai S, Mukherjee A. Epithelial mesenchymal transition in lung cancer cells: A quantitative analysis. Annu Int Conf IEEE Eng Med Biol Soc. 2015;2015:5372–5.
69. Zou H, Yang Z, Chan YS, Yeung SA, Alam MK, Si T, et al. Single cell analysis of mechanical properties and EMT-related gene expression profiles in cancer fingers. iScience. 2022;25(3):103917.
70. Reader J, Holt D, Fulton A. Prostaglandin E2 EP receptors as therapeutic targets in breast cancer. Cancer Metastasis Rev. 2011;30(3–4):449–63.
71. Majumder M, Nandi P, Omar A, Ugwuagbo KC, Lala PK. EP4 as a therapeutic target for aggressive human breast Cancer. Int J Mol Sci. 2018;19(4).
72. Cheng SY, Zhang H, Zhang M, Xia SK, Bai XM, Zhang L, et al. Prostaglandin E(2) receptor EP2 mediates snail expression in hepatocellular carcinoma cells. Oncol Rep. 2014;31(5):2099–106.
73. Urban J, Kuzbicki L, Szatkowski G, Stanek-Widera A, Lange D, Chwirot BW. Stromal, rather than epithelial cyclooxygenase-2 (COX-2) expression is associated with overall survival of breast cancer patients. BMC Cancer. 2014;14:732.
74. Mhaidly R, Mechta-Grigoriou F. Fibroblast heterogeneity in tumor micro-environment: role in immunosuppression and new therapies. Semin Immunol. 2020;48:101417.
75. Li A, Chen P, Leng Y, Kang J. Histone deacetylase 6 regulates the immunosuppressive properties of cancer-associated fibroblasts in breast cancer through the STAT3-COX2-dependent pathway. Oncogene. 2018;37(45):5952–66.
76. Karavitis J, Hix LM, Shi YH, Schultz RF, Khazaie K, Zhang M. Regulation of COX2 expression in mouse mammary tumor cells controls bone metastasis and PGE2-induction of regulatory T cell migration. PLoS ONE. 2012;7(9):e46342.
77. Janus P, Kus P, Jaksik R, Vydra N, Toma-Jonik A, Gramatyka M, et al. Transcriptional responses to direct and indirect TGFB1 stimulation in cancerous and noncancerous mammary epithelial cells. Cell Commun Signal. 2024;22(1):522.
78. Wu J, Zhang Y, Frilot N, Kim JI, Kim WJ, Daaka Y. Prostaglandin E2 regulates renal cell carcinoma invasion through the EP4 receptor-Rap GTPase signal transduction pathway. J Biol Chem. 2011;286(39):33954–62.

Publisher's note